

# Atom Probe Tomography Analysis of SiGe Fins Embedded in SiO<sub>2</sub>: Facts and Artefacts

D. Melkonyan<sup>\*,\*\*</sup>, C. Fleischmann<sup>\*\*</sup>, L. Arnoldi<sup>\*,\*\*</sup>, J. Demeulemeester<sup>\*\*</sup>, A. Kumar<sup>\*,\*\*</sup>, J. Bogdanowicz<sup>\*\*</sup>, F. Vurpillot<sup>\*\*\*</sup> and W. Vandervorst<sup>\*,\*\*</sup>

\* Instituut voor Kern- en Stralingsfysica, KU Leuven, Celestijnenlaan 200D, B-3001 Leuven, Belgium

\*\* Imec vzw, Kapeldreef 75, Heverlee – 3001, Belgium

\*\*\* GPM, UMR 6634 CNRS, Université et INSA de Rouen, 76801 Saint-Etienne du Rouvray Cedex, France

## Abstract

We present atom probe analysis of 40 nm wide SiGe fins embedded in SiO<sub>2</sub> and discuss the root cause of artefacts observed in the reconstructed data. Additionally, we propose a simple data treatment routine, relying on complementary transmission electron microscopy analysis, to improve compositional analysis of the embedded SiGe fins. Using field evaporation simulations, we show that for high oxide to fin width ratios the difference in evaporation field thresholds between SiGe and SiO<sub>2</sub> results in a non-hemispherical emitter shape with a negative curvature in the direction across, but not along the fin. This peculiar emitter shape leads to severe local variations in radius and hence in magnification across the emitter apex causing ion trajectory aberrations and crossings. As shown by our experiments and simulations, this translates into unrealistic variations in the detected atom densities and faulty dimensions in the reconstructed volume, with the width of the fin being up to six-fold compressed. Rectification of the faulty dimensions and density variations in the SiGe fin was demonstrated with our dedicated data treatment routine.

Keywords: atom probe tomography; tip shape; FinFET; local magnification; trajectory overlaps.

## 1. Introduction

Atom probe tomography (APT) can yield quantitative 3D elemental information at the sub-nanometer scale on a variety of materials systems.<sup>1,2</sup> It relies on the controlled (voltage or laser-pulsed) field-ionization and evaporation of surface atoms from a needle-shaped specimen, typically with an apex radius of about 50-100 nm. The evaporated ions are accelerated by the applied electric field toward a position sensitive detector providing spatial information on the point of emission. By measuring the time-of-flight of the ions, their mass to charge ratio can be obtained, which allows to identify different atoms. The full 3D information, i.e. the original  $x$ ,  $y$  and  $z$  position of the atoms inside the specimen is derived from a volume reconstruction by applying a simple stereographic projection model,<sup>3,4</sup> which assumes a hemispherical specimen apex shape and relies on the sequential evaporation of the atoms from the apex surface. The reconstruction process of an atom probe data set is commonly performed using either the SEM image of the emitter (before and after the measurement), the cone angle approximation<sup>3</sup> or the applied voltage, which is directly proportional to the emitter radius during analysis.<sup>5</sup> In view of the limited conductivity of most semiconductor structures, laser-assisted evaporation has become the standard for these applications.<sup>6</sup>

Clearly, the 3D-resolving power and element identification properties of laser-assisted APT holds large promises for the composition and dopant analysis of nanoscaled semiconductor devices<sup>2,7</sup> such as MOSFETs,<sup>8</sup> finFETs<sup>9</sup> and Gate-all-around<sup>10</sup> devices. However, these devices are inherently very complex due to their 3D architecture and due to the confinement of different type of materials (semiconductors, oxide, metals) into very small volumes (a few tens of nanometer). The heterogeneity of these systems bears several challenges to the APT analysis linked to the sample preparation (based on focused ion beam based techniques ),<sup>11</sup> the evaporation and data reconstruction.<sup>10,12</sup> Problems arise during specimen preparation due to the differences in sputtering and amorphization depth and range during ion milling<sup>13</sup>, which sometimes can be bypassed using e.g. de-processing.<sup>14</sup> On the contrary, non-homogenous laser absorption<sup>15</sup> and/or differences in the evaporation field thresholds ( $F_{evap}$ )<sup>16</sup> in a heterogeneous specimen are of much more fundamental nature as this may cause a non-hemispherical specimen shape during field evaporation.<sup>15,16</sup> With local variations in the specimen radius across the surface, the electric field, the ion trajectories and hence the magnification are non-constant across the specimen surface, rendering simple point projection models inadequate and the resulting volume reconstruction faulty.<sup>17</sup> Severe shape and dimension distortions<sup>16,18,19</sup> or intermixed interfaces<sup>17,19</sup> are a typical consequence of this. Detailed information about the specimen surface shape (evolution) during APT analysis is therefore a necessary prerequisite to obtain a correct reconstructed volume and composition. However, for complex systems this information cannot simply be deduced from a (static) detector hit map, as Larson *et al.* has pointed out.<sup>20,21</sup> In this respect developing a dedicated instrument combining the APT and transmission electron microscopy (TEM) can help to monitor the emitter shape during field evaporation in future.<sup>22</sup> If the specimen surface shape is obtained from field-evaporation simulation one should account for the fact that the specimen properties may not always be symmetric around its axis. Consequently, the specimen shape may evolve differently in the  $x$  direction than in the  $y$  direction, as will be shown below. In the current work, we study the distortions and artefacts induced during the analysis of a 40 nm wide SiGe fin embedded in SiO<sub>2</sub>. With field evaporation simulations, we explore the evolution of the specimen shape and its resultant surface projection and gain insight into the root-causes of the observed artefacts in the reconstructed data. Furthermore, by correcting the APT reconstructed volume with dimensional information obtained from TEM analysis, we have developed a method that corrects for some of the artefacts and extracts compositional profiles across the fin in line with TEM-EDX results.

## 2. Experimental

The test structure consists of 40 nm wide, 130 nm high and 10  $\mu$ m long Si<sub>0.3</sub>Ge<sub>0.7</sub> fins with a pitch of 400 nm, which were grown on a Si substrate into patterned trenches with vertical SiO<sub>2</sub> sidewalls (shallow trench isolation) and capped with strained Ge layer (sGe) (Fig. 1a). After capping, the substrate was chemically mechanically-polished (CMP). Epitaxial growth was done by means of Chemical Vapor Deposition using a production compatible ASM Epsilon3200 tool. Relaxed SiGe was grown at a nominal temperature of 525 °C. The growth temperature of sGe was lower to maintain two-dimensional growth (to avoid 3D growth). The content of Ge was measured by means of Energy-dispersive X-ray spectroscopy and High Resolution X-Ray Diffraction Reciprocal Space Mapping measurements.<sup>23,24</sup> The TEM specimens were prepared using a focused ion beam (FIB; Helios 450HP), and characterized at 120 kV using a double-corrected FEI Titan 60-300 Cube TEM/STEM, containing a superX EDS system (Bruker) (Fig. 1b). A 50 nm amorphous Si cap layer (not shown) was sputter-deposited using a Gatan PECS682 coating system, to prevent the FIB-induced Ga<sup>+</sup> ion beam damage<sup>25</sup> during APT specimen preparation (standard lift out technique)<sup>11</sup>. APT analysis was performed with a Laser Assisted Wide Angle Atom Probe (LAWATAP, CAMECA). The sample base temperature was set to 80 K and the

detection rate was kept constant at 0.005 atoms/pulse throughout the experiment. We used an UV laser ( $\lambda = 343$  nm) with a spot size of approximately 100  $\mu\text{m}$ , a laser pulse energy of 0.18  $\mu\text{J}$  and a pulsing frequency of 10 kHz, yielding a 9 to 1 single to double charged Ge ratio. The TAP3D reconstruction software was used to reconstruct the 3D volume of the sample. We assigned the peaks at 9.3, 9.7 and 10 Da to  $\text{Si}^{+++}$  ions, 14, 14.5 and 15 Da to  $\text{Si}^{++}$  ions and 28,29 and 30 Da peaks to  $\text{Si}^+$  ions. The peaks at 35, 36, 36.5, 37, 38 Da were assigned to  $\text{Ge}^{++}$  ions and those at 70,72,73,74,76 Da to  $\text{Ge}^+$  ions. No SiGe molecular ions were detected. The peaks at 16 and 32 Da were assigned to  $\text{O}^+$  and  $\text{O}_2^+$  ions, respectively and the peaks at 44 and 60 Da were identified as  $\text{SiO}^+$  and  $\text{SiO}_2^+$  respectively. Field evaporation simulations were performed with the software developed by Vurpillot *et al.*<sup>26,27</sup> Several studies have proven its ability to qualitatively predict experimental emitter shapes (and their evolution) and ion trajectories in complex multilayer systems.<sup>10,28</sup> In this simulation, each atom is represented as a conductive cube in a cubic lattice. These “atoms” are confined inside a cylindrical envelope with a 20 nm radius terminated with a hemispherical cap. The simulated emitter has no shank angle and is kept at a uniform temperature. No thermal pulses linked to laser-tip interactions are considered in the simulation. The electric potential above the tip was derived by numerically solving the Laplace equation in the space, free of charge ( $\Delta V = 0$ ). This potential was used to obtain the electric field and the Newton’s second law of motion, ( $F = eE = md^2r/dt^2$ ) was applied to calculate the trajectories of ions close to the tip surface. A spherical electrode at ground potential is positioned 20 nm away from the emitter surface to create the required electric field distribution around the tip. For interpreting the data, we assume that beyond the ground electrode the ions are linearly projected onto the detector along the direction of their velocity vector. To circumvent the mismatch in dimensions between the experimental emitter radius (>50 nm) and the simulated emitter radius (17.5 nm), we have downscaled the experimental structure.

### 3. Results and discussion

#### 3.1 Fin width and Ge concentration profiles

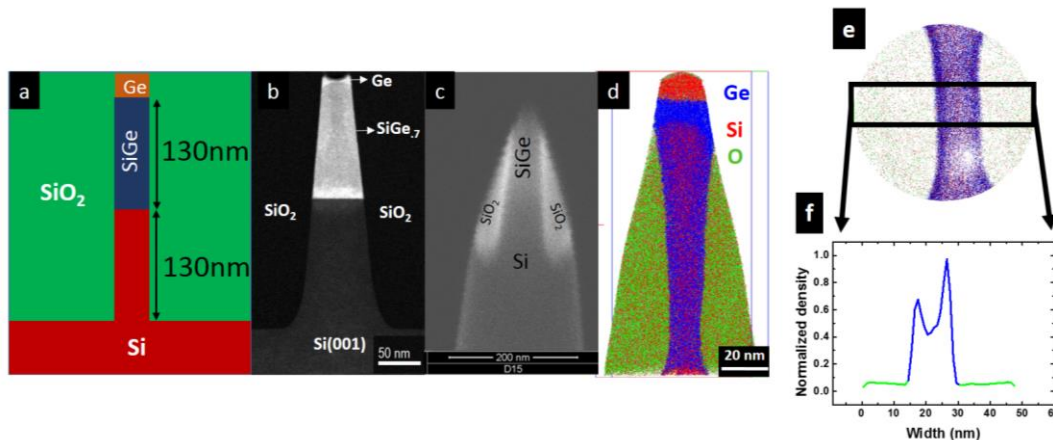


Fig. 1. (a) Schematic representation and (b) cross-sectional high-angle annular dark-field scanning TEM image of the SiGe fin investigated in this study. (c) SEM image of the APT specimen prepared from the SiGe fin shown in (b) before analysis. (d) 3D reconstructed APT data using the standard voltage-based reconstruction scheme. The blue, red and green dots represent the Ge, Si and O atoms, respectively. The fin width is smaller in the reconstructed volume compared to the actual fin width as deduced from (b). This

artefact becomes more pronounced with depth. (e) A selection of a volume with 2 nm thickness in z-direction taken at 55 nm depth along the xy plane of the reconstructed data. (f) Atom density (sum of all atoms) as measured across the SiGe fin (indicated by the black box) revealing a substantial density differences between the SiO<sub>2</sub> (green) and SiGe (blue) region, which is more pronounced at the fin/oxide interface.

Figure 1(c) shows the SEM image of a needle-like tip before APT analysis, with the SiGe fin in the center of the tip. The 3D image of the analyzed volume after data reconstruction is presented in Fig. 1(d). Both, standard voltage-based (Fig. 1d) and tip geometry-based reconstruction algorithms yield the same results. We have chosen the reconstruction parameter, i.e. image compression<sup>3</sup> and field reduction factors,<sup>29</sup> to match the height (130 nm) of the SiGe fin with the TEM measurements (Fig. 1b). A comparison of the APT reconstructed volume (Fig. 1d) with the TEM image (Fig. 1b) reveals severe spatial distortions and a much smaller Fin width in the APT volume. Remarkably, the fin width becomes increasingly smaller (i.e. compressed) further away from the fin surface. Whereas at the surface the fin width is half the size measured from the TEM image, it is one sixth of the width at the bottom. This is substantiated by an increased oxide to fin width ratio at the bottom of the APT specimen compared to its top (Fig. 1c). As will be discussed below (Fig. 5), this ratio determines the degree of tip shape deformation and hence the compression of the fin width (i.e. variation in magnification). In addition, an anomalous high atom density in the SiGe fin region, particularly at the fin-oxide interface, is visible in the cross-sectional top-view of the reconstructed volume (Fig. 1e) and the atom density plot taken across the fin (Fig. 1f). In detail, the atom density difference between the SiGe fin and the SiO<sub>2</sub> region exceeds the expected value by a factor 10.

As verified by our field evaporation simulations (Fig. 2 and 4), these artefacts originate from a non-hemispherical specimen shape, which in turn causes different magnifications over the specimen surface rendering the standard reconstruction models to fail as they are based on uniform magnifications. To validate this point we have performed simulations of the tip shape evolution for an initial structure as shown in Fig. 2. Basically, the structure consists of a low  $F_{\text{evap}}$  layer (Fig. 2a blue) sandwiched between two high  $F_{\text{evap}}$  layers (Fig. 2a green), representing the SiGe fin and SiO<sub>2</sub> layers, respectively. In essence the simulation program<sup>26,27</sup> searches at each iteration point for the atom(s) with the highest probability for evaporation. At present, it uses as input the ratio between the evaporation fields rather than absolute  $F_{\text{evap}}$  numbers to calculate and weigh the probability for an atom to evaporate from the surface. In this study a  $F_{\text{evap}}(\text{SiO}_2)$  to  $F_{\text{evap}}(\text{SiGe})$  ratio of 1.8 yields the best quantitative agreement between the experimental and simulated results in view of the emitter shape and the relative fin compression in the reconstructed volume. A good qualitative agreement was found for all ratios between 1.4 to 2.2. In case the tip has a uniform temperature distribution, the simulations outlined here only account for differences in  $F_{\text{evap}}$ . However, in case a non-uniform temperature distribution would exist for instance as a result of the local interaction between the tip surface and the applied laser light (leading to local differences in laser light absorption and/or thermal conductivity<sup>15</sup>), the differences in local temperature would translate into a higher (lower) probability of evaporation. Hence such effects can equally well (indirectly) be accounted for by the input value of the field ratio. We acknowledge that in such a case the input ratio in “evaporation fields” does not merely reflect the material properties but describes the combined effect of a higher/lower temperature and evaporation field. In other words, by increasing the  $F_{\text{evap}}$  ratio between the SiGe and SiO<sub>2</sub> region, a temperature gradient between both phases would be accommodated in the simulations.

Figure 2 a-d and f-i show the simulated emitter shape evolution taken in cross-sections across (x direction) and along the fin (y direction), respectively. Initially, atoms from the fin region (blue region) are preferentially evaporated due to their lower evaporation field threshold compared to the atoms in the SiO<sub>2</sub> (green region). At this point, the fin region becomes flat in x direction (Fig. 2 b). If evaporation proceeds, the low  $F_{\text{evap}}$  region develops a concave radius (negative curvature), while the high  $F_{\text{evap}}$  region remains convex (Fig. 2c). In the further course of simulation, i.e. the emitter surface moved approximately 10 nm, an equilibrium emitter shape is established that maintains a concave curvature (Fig. 2d), in good agreement with the experimentally observed emitter shape (after APT analysis) shown in Fig. 2k. In contrast to the x direction, no vertical interfaces (i.e. different  $F_{\text{evap}}$ ) exist in y direction and hence the emitter shape changes only slightly, with no abrupt variations in the radius over the surface (Fig. 2f-i). This is true for different cross-sections taken along the Y direction, away from the emitter center axis (Fig. 2j).

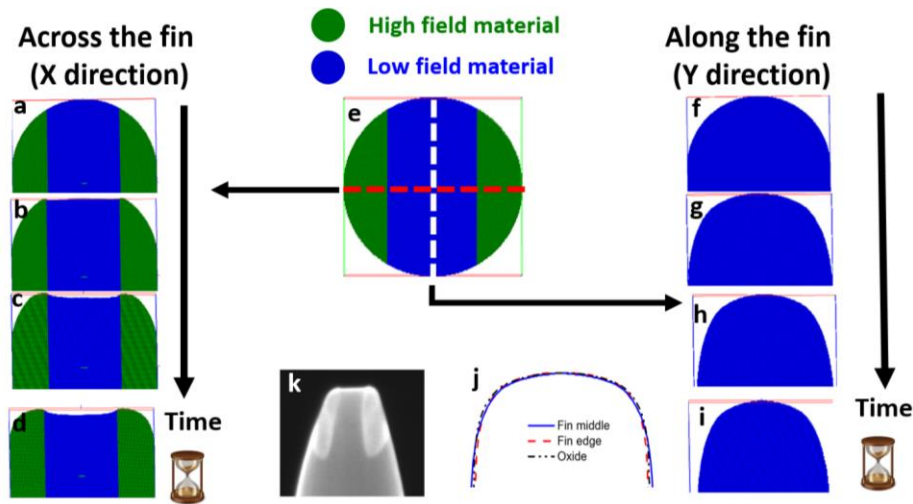
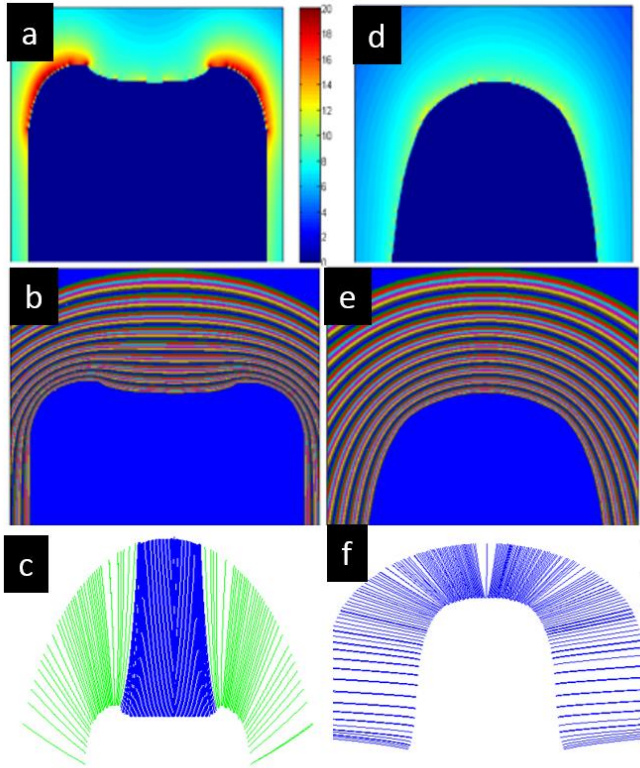


Fig.2 Emitter shape evolution during the field evaporation. Cross-sections were taken across the fin (x direction) (a-d) and along the fin (y direction) (f-i), after evaporation of approximately 4 nm (b), 7 nm (c) and 10 nm (d) from the initial emitter surface. (e) Top view of the simulated structure. The dashed lines indicate where the cross-sections shown in (a-d) and (f-i) were taken. (j) Radius of the simulated emitter at the equilibrium state in y direction as shown in (i) taken at the middle of the fin (blue), at the edge of the fin (i.e. 0.5 nm away from fin-oxide interface) (red) and in the SiO<sub>2</sub> region (i.e. 0.5 nm away from fin-oxide interface). (k) SEM image of an experimental emitter shape after APT analysis.

The computed electric field and potential distribution at this equilibrium emitter apex (Fig. 2d, i) are presented in Fig. 3a, d and b, e, respectively. As expected, along the y direction the electric field remains uniform (except for the higher field at atomic kink sites) across the emitter surface (Fig. 3d) and the equipotential lines are solely convex (Fig. 3e). In the x direction, the most striking observations are the electric field enhancement at the apex above the SiO<sub>2</sub> region (Fig. 3a) as well as the peculiarly shaped equipotential lines, which are concave above the fin region, i.e. the region with negative curvature (Fig. 3b). With increasing distance from the emitter surface this trend diminishes. The resultant ion trajectories are shown in Fig. 3 c, f. Assuming the ions have no initial velocity, they will follow the electric field lines (not shown), which are perpendicular to the equipotential lines, at their initial stage of departure.<sup>30</sup> Hence,

immediately above the fin region (and in particular above the fin-SiO<sub>2</sub> interface) ion trajectories diverge much less compared to those above the SiO<sub>2</sub> region, given the concave-shaped equipotential lines (in x direction). As the ion trajectories deviate from those observed for an ideal, hemispherical emitter surface, this phenomenon is commonly referred to as ion trajectory aberrations.<sup>31</sup> Further away from the tip apex, the electric field is reduced and the equipotential lines are everywhere convex (Fig. 3b,e) resulting in diverging ion trajectories that are primarily determined by the ion's velocity vectors. The important point to note is that due to the influence of the emitter shape on the ion trajectories in x direction, the image formed by the impacting ions on the detector will be less magnified in the fin region than in the SiO<sub>2</sub> region (Fig. 3c). In other words, the magnification differs across the emitter surface due to local differences in tip radii. As a result, the detected atom density will be spatially dependent as well (Fig. 4a, b). For areas with high negative curvature such as at the fin-oxide interface, crossing of ion trajectories (Fig. 4c, d) might even occur leading to a complete deterioration of the spatial resolution. In the y direction, the image is projected with a constant magnification over the surface (Fig. 3f) with the exception of the known gaps linked to the crystallographic poles.<sup>32</sup>



*Fig. 3. Electric field distribution around the tip (in equilibrium state) in x direction (a) and y (d) direction. Equipotential lines between the emitter apex and the counter electrode in x direction (b) and y (e) direction. Trajectories of ions evaporated from an atomic row on the emitter apex in x direction (c) and y direction (f). In (c) green lines indicate trajectories for ions from the SiO<sub>2</sub> region, blue for ions from the fin region.*

Note that our field evaporation simulations accurately reproduce the experimentally observed compression in the fin region along the x direction, including the high density regions at the fin-oxide interface (Fig. 4b, 1f). In the simulations the apparent fin width (6 nm) is roughly  $\sim 3$  times smaller as compared to the real value (18 nm). Such a compression is similar to our experiments where a 40 nm fin was compressed to 13 nm. The simulations also reproduced the density variations in the entire volume including the unrealistic low density of  $\text{SiO}_2$  compared to the fin and the high density areas at the fin-oxide interfaces (Fig. 4b, 1f). From the simulations it becomes clear that the latter originate from the concave emitter shape at the fin/oxide interface (Fig. 2d), which leads to highly condensed ion trajectories in this region (Fig. 4c, d) and thus an apparently increased atom density.

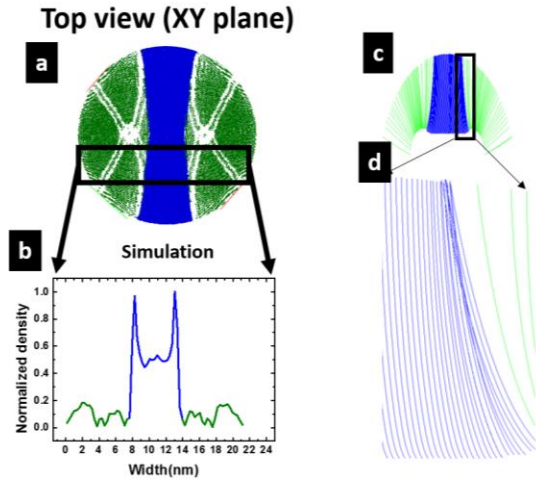


Fig. 4. (a) Top view of the simulated reconstructed data, where blue is the low evaporation field material (fin) and green is the high evaporation field material (oxide). (b) Atom density across the low evaporation field material in the simulated reconstructed data. (c) Ion trajectories of the surface atoms in x direction (across the fin). (d) Close-up view of the fin/oxide interface as indicated by the black box in (c).

As mentioned before, the effective compression in the x dimension varies throughout the depth of the analyzed volume (z direction), implying that the  $F_{\text{evap}}$  ratio is not the only parameter critical to the emitter shape evolution. Indeed, in the real structure the width of the fin increases with depth (Fig. 1b) while the oxide thickness (in function of z) is determined by the cone angle of the APT specimen. As visible from Fig. 1c, the oxide width increases at a faster rate than the width of the fin, resulting in a different oxide to fin width ratio at the bottom of the structure as opposed to the surface. To understand its impact on the apparent fin width, we performed field evaporation simulations in which the fin width (blue region in Fig. 2) was kept constant, while the oxide width (green region in Fig. 2) was gradually increased and vice versa. We quantify the results using a *compression factor* (CF), which is defined as the ratio of the actual fin width to the (compressed) fin width obtained in the reconstructed volume. Based on the results summarized in Fig. 5 it is clear that the oxide to fin width ratio, at a fixed fin and oxide evaporation field, is the determining parameter for the compression factor and hence controls the degree of concavity of the tip surface (Fig. 5a, b and c, d). A small CF is only observed for oxide to the fin width ratios  $\sim 0.5$ , as is the case in the top part of the APT specimen, implying minimal compression. With increasing material removal, the tip contains more and more oxide and hence the oxide to fin width ratio will increase. Thus,

the CF increases significantly and the compression of the fin increases (up to 6x) causing the apparent reduction (6x) in fin width in the reconstructed volume (Fig. 1d).

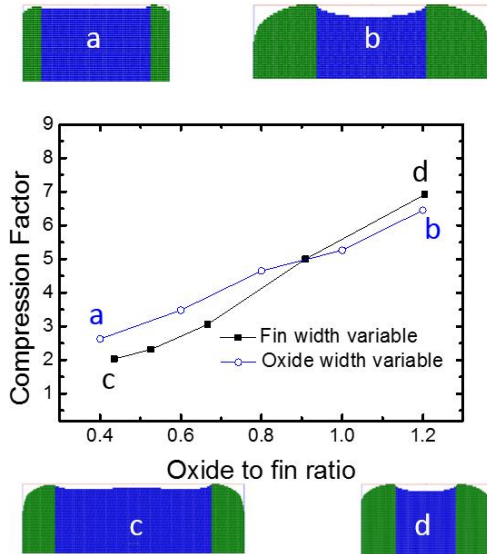


Fig. 5 The impact of the oxide to fin width ratio on the fin compression. Depending on fin to oxide width ratio, the tip shape within the fin transitions from flat (a) and (c) (for small oxide to fin ratios) towards concave (b) and (d) (for large oxide to fin ratios).

Unfortunately these local magnification variations over the emitter surface are not accounted for in standard reconstructions schemes and thus lead to erroneous dimensions in the reconstructed volume as well as density variations (Fig. 1d, f). It has been shown<sup>33,34</sup> that such artefacts can be corrected using density correction algorithms as implemented in commercially available reconstruction softwares (e.g. IVAS or TAP3D).<sup>35</sup> Shortly, in these algorithms the reconstructed volume is divided into small sub-volumes and the atom density in each sub-volume is calculated. The density correction is performed iteratively by slightly expanding the sub-volumes with high atom density and compressing the sub-volumes with low atom density, allowing a maximum change of 10% per each sub-volume. Grenier *et al.* have recently demonstrated that this method, particularly when combined with correlative microscopy, can be successfully applied to improve data reconstruction of complex nanostructures in view of dimensions and anomalous density variations, providing strong ion intermixing resultant from trajectory overlaps can be excluded.<sup>10,12,28</sup> As will be discussed in more detail below, the latter is also true in our study, where ion intermixing is less than 1.3%. Moreover, we have proven above that the density variations in our data are unidirectional, i.e. confined to the x-direction, which allows us to apply a computationally less intense algorithm to correct for the observed artefacts in the reconstructed volume as was suggested by Sauvage *et al.*<sup>34</sup> In more detail, we choose a square selection in the x-y plane of 2 nm thickness at a fixed depth (Fig. 6). From this selection, the fin region is divided into uniform rectangular cells of 0.5 nm width ( $W_{cell}$ ) in the x direction (Fig. 6b). Each cell is unidirectionally expanded along the x direction to obtain a uniform density over the complete fin region (i.e. over all cells) (Fig. 6c) until the actual fin width ( $W_{TEM}$ ) is obtained, which is known from complementary TEM analysis. The expansion of each cell is based on a one-directional enlargement coefficient ( $EC$ ):

$$EC = \frac{N_{cell}}{N_{total}} \frac{W_{TEM}}{W_{cell}}$$

which is linearly proportional to the number of atoms in the cell ( $N_{cell}$ ) to be expanded, relative to the total number of atoms over all cells (in the fin region) of the selected volume ( $N_{total}$ ). The corrected cell width ( $W_{cell\_correct}$ ) is obtained by multiplying the original cell width ( $W_{cell}$ ) by its compression factor EC:

$$W_{cell\_correct} = EC * W_{cell}$$

In other words, the cell with the highest atomic content will be expanded the most and vice versa, as indicated in Fig. 6b, c. Note that a too small  $W_{cell}$  will increase the statistical error due to the low number of atoms contained in each cell, while with a very large  $W_{cell}$  density variations will not be rectified.

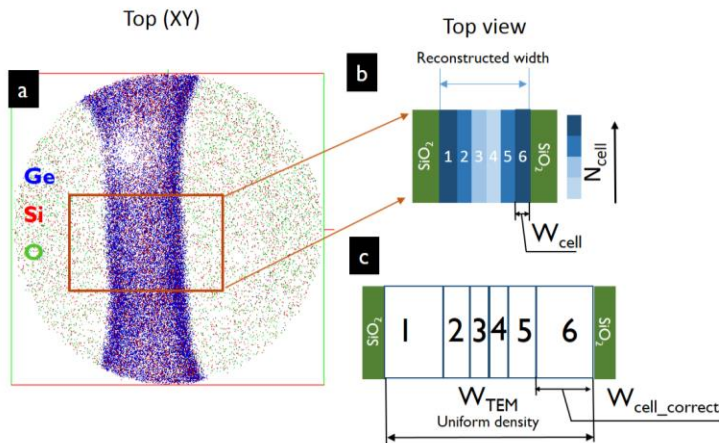


Fig. 6. 1D density correction principle. (a) A selection of a volume with 2 nm Z (taken at 55 nm) along xy plane, of reconstructed SiGe fin embedded in SiO<sub>2</sub>. (b) Schematic representation of a top view of a SiGe fin (blue) embedded in SiO<sub>2</sub>, before the density correction. Here the SiGe fin is divided into cells along the y dimension where the higher density is depicted with darker shade. (c) Schematic representation of a top view of a SiGe fin embedded in SiO<sub>2</sub>, after the density correction.

Figure 7a shows the reconstructed volume after the density correction, the 2D Ge concentration distribution in the SiGe fin in the xz plane (Fig. 7b) and the 1D Ge compositional profile (Fig. 7c, squares) across the SiGe fin (at z=55 nm depth). Near the edges close to the top of the fin there are clearly Ge enriched areas where the Ge content is more than 10% higher as compared to the middle of the fin, which becomes less pronounced with increasing depth (Fig. 7b). This behavior is consistent with the variations seen in the TEM image in Fig. 1.b, where the edges of the fin also have a brighter contrast corresponding to a higher Ge content. Note that the TEM analysis was performed on a standard TEM lamella, and not on the APT conical specimen itself. In addition, the overlay of the 1D Ge concentration profile across the fin (at z=55nm depth) as obtained with TEM/EDS and APT shows an excellent agreement (Fig. 7 c), indicating the accuracy of the proposed correction algorithm.

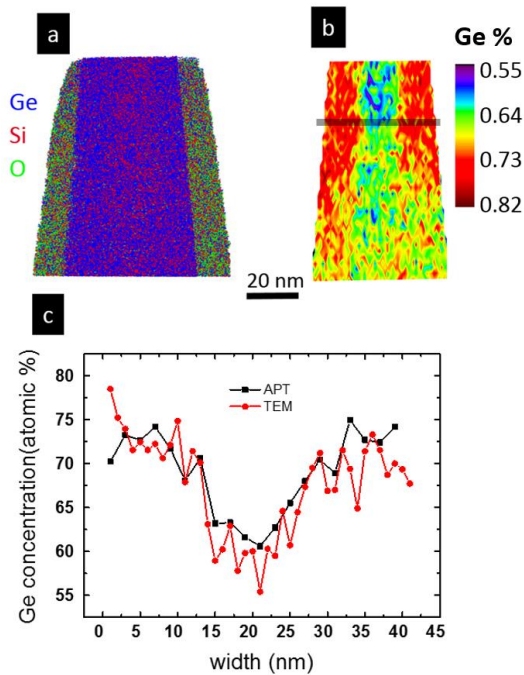


Fig. 7. (a) SiGe fin embedded in SiO<sub>2</sub> after the density correction. (b) Ge concentration across the fin (x-z plane) after the density correction. The black horizontal line indicates the location where the 1D profile in (c) is measured. (c) 1D Ge concentration profile across the SiGe fin as measured with APT (black) and TEM (red) revealing a higher Ge content at the edges of the Fin as compared to the middle.

As Richard et al. has pointed out, the Ge enrichment at the edges of the fin arises from an increased Ge incorporation rate at {111} facets, originating from growth rate difference perpendicular to {111} and {001} facets.<sup>36</sup>

### 3.2 Trajectory overlap

A detailed analysis of the trajectories calculated in Fig. 4c, d indicates that at the edges of the SiO<sub>2</sub>/SiGe interface, there is a finite probability that ions from a neighboring region (SiO<sub>2</sub>) get projected onto the other region (SiGe). This arises from the concave tip shape at this interface. When analyzing the oxygen

distribution map for the present case, it is clear that some oxygen atoms appear to be located in the SiGe region (Fig. 8b). Since from a processing point of view, the SiGe should be free of any oxygen content, Fig. 8b clearly indicates that oxygen atoms originating from the SiO<sub>2</sub> are detected within the fin region. Note that since this concave shape only exists in the SiGe region and not in the SiO<sub>2</sub> penetration of Ge into the SiO<sub>2</sub> region is far less pronounced and defined by the overall spatial resolution of APT (Fig. 8c).

While the density correction solves the problem of the fin dimensions, it is not able to correct these ion trajectory overlaps.<sup>17,19</sup> In these cases, spatial information is lost and cannot be restored. Hence as ions (Si, O) from the SiO<sub>2</sub> region will intermix in the adjacent SiGe phases, the compositional analysis (in particular the Si:Ge ratio) in the SiGe will be influenced as well. The magnitude of this effect can be estimated by considering the 1D compositional profile of the O atoms across the fin at z=55 nm depth (Fig. 8c). At the edges of the SiGe fin, the oxygen content is about 2%, which becomes negligible (less than 0.2%) in the middle of the fin. Hence assuming that Si atoms from the SiO<sub>2</sub> also get added to the SiGe fin with a similar efficiency as the oxygen atoms and considering the measured Si concentration in the SiO<sub>2</sub> (versus oxygen, 2:3), we can find that at the edge of the fin the Si concentration is overestimated with 1.3%, again decaying into the middle of the fin to 0.13%. Accounting for this effect would increase the Ge-concentration at the fin-edge from 73 % towards 74 % which is still within the statistical errors of APT quantification. Moreover, the rapid decay of the Si-overestimate with distance towards the center (similar to the oxygen profile in Fig. 8c), implies that the observed non-uniformity of the Ge within the fin is real and not an APT artefact. This argument is further substantiated by the good agreement with the TEM results (Fig. 7c).

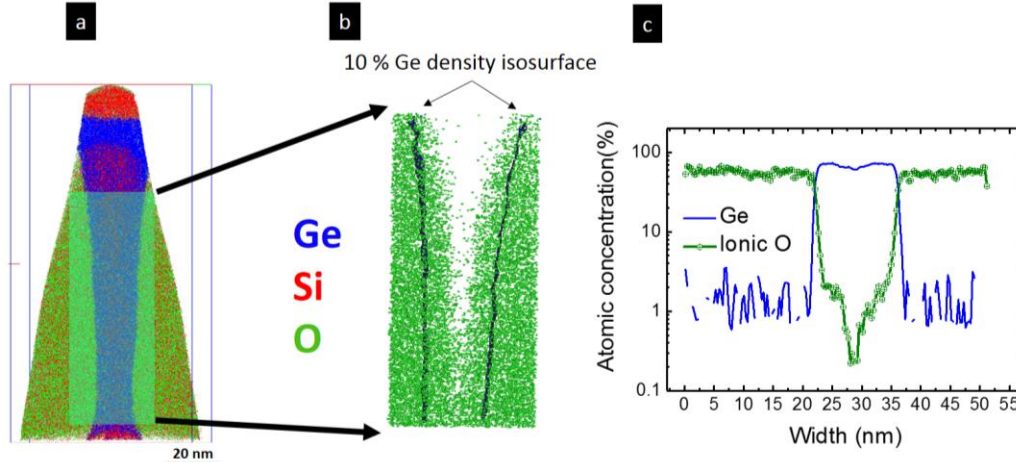


Fig. 8 (a,b) Oxygen atoms detected in the SiGe fin in the reconstructed volume as a result of ion trajectory overlaps. (b) The two black 'lines' along the z direction represent 10 % Ge iso-concentration surfaces separating the fin (Si<sub>0.3</sub>Ge<sub>0.7</sub>) from the oxide (SiO<sub>2</sub>). The green dots represent O<sup>+</sup> and O<sub>2</sub><sup>+</sup> ions. Those located in between the Ge iso-concentration surfaces are oxygen atoms detected in the fin as a result of overlapping ion trajectory. (c) 1D profile of Ge and O content across the fin.

## 4. Conclusions

The potential errors and artefacts occurring during the APT analysis of a SiGe fin embedded in SiO<sub>2</sub> were studied. Our experimental results show that one suffers from local magnification variations as well as

trajectory overlaps leading to erroneous dimensions and the intermixing of different phases. Using theoretical simulations of tip shape evolution and the associated ion trajectories, we were able to show that the tip develops a concave surface morphology across the fin while it remains convex along the fin during the field evaporation. The origin of this evolution lies in the large differences in the threshold evaporation field between the fin (SiGe) and the oxide (SiO<sub>2</sub>) material. As a consequence of this peculiar tip shape evolution, unidirectional (across the fin) focusing of the fin ions trajectories is observed, inducing severe magnification reduction in that direction. This results in smaller fin width and anomalous atom density variations in the reconstructed volume. Moreover, crossing of the trajectories across the fin are also observed, inducing intermixing of fin and oxide ions and inducing erroneous spatial distribution and quantification. As they cannot be corrected, a quantitative analysis of the impact of the trajectory overlap was made, indicating that the Ge concentration at the edges of the fin is underestimated with <1.3 %. We also showed that the oxide to fin width ratio is the detrimental factor whereby these artefacts become more pronounced when this ratio increases. A density correction algorithm was developed which, using dimensional information from the TEM image of the fin, removes the fin compression and the density variations. In the corrected data we observed high Ge content in the middle of the fin compared to its edges, which was in a good agreement with the data obtained by EDS/TEM.

## Acknowledgements

We gratefully acknowledge the funding for this work through the European Metrology Programme for Innovation and Research (EMPIR) Project 3DMetChemIT. The EMPIR initiative is co-funded by the European Union's Horizon 2020 research and innovation programme and the EMPIR Participating States.

1. Amouyal, Y. & Schmitz, G. Atom probe tomography—A cornerstone in materials characterization. *MRS Bull.* **41**, 13–18 (2016).
2. Kelly, T. F. & Larson, D. J. Atom Probe Tomography 2012. *Annu. Rev. Mater. Res.* **42**, 1–31 (2012).
3. Gault, B. *et al.* Advances in the reconstruction of atom probe tomography data. *Ultramicroscopy* **111**, 448–457 (2011).
4. Bas, P., Bostel, A., Deconihout, B. & Blavette, D. A general protocol for the reconstruction of 3D atom probe data. *Appl. Surf. Sci.* **87–88**, 298–304 (1995).
5. R. Gomer. Field emission and field ionisation Harvard. (1961).

6. Gault, B. *et al.* Design of a femtosecond laser assisted tomographic atom probe. *Rev. Sci. Instrum.* **77**, 043705 (2006).
7. Kelly, T. F. *et al.* Atom Probe Tomography of Electronic Materials. *Annu. Rev. Mater. Res.* **37**, 681–727 (2007).
8. Inoue, K. *et al.* Dopant distributions in n-MOSFET structure observed by atom probe tomography. *Ultramicroscopy* **109**, 1479–1484 (2009).
9. Kambham, A. K., Kumar, A., Gilbert, M. & Vandervorst, W. 3D site specific sample preparation and analysis of 3D devices (FinFETs) by atom probe tomography. *Ultramicroscopy* **132**, 65–69 (2013).
10. Grenier, A. *et al.* 3D analysis of advanced nano-devices using electron and atom probe tomography. *Ultramicroscopy* **136**, 185–192 (2014).
11. Miller, M. K., Russell, K. F., Thompson, K., Alvis, R. & Larson, D. J. Review of Atom Probe FIB-Based Specimen Preparation Methods. *Microsc. Microanal.* **13**, 428–436 (2007).
12. Gilbert, M., Vandervorst, W., Koelling, S. & Kambham, A. K. Atom probe analysis of a 3D finFET with high-k metal gate. *Ultramicroscopy* **111**, 530–534 (2011).
13. Panciera, F. *et al.* Atom probe tomography of SRAM transistors: Specimen preparation methods and analysis. *Microelectron. Eng.* **107**, 167–172 (2013).
14. Ajay Kumar Kambham, KULeuven, 2014.
15. Koelling, S. *et al.* In-situ observation of non-hemispherical tip shape formation during laser-assisted atom probe tomography. *J. Appl. Phys.* **109**, 104909 (2011).
16. Marquis, E. A., Geiser, B. P., Prosa, T. J. & Larson, D. J. Evolution of tip shape during field evaporation of complex multilayer structures: EVOLUTION OF TIP SHAPE DURING FIELD EVAPORATION. *J. Microsc.* **241**, 225–233 (2011).
17. Vurpillot, F., Bostel, A. & Blavette, D. Trajectory overlaps and local magnification in three-dimensional atom probe. *Appl. Phys. Lett.* **76**, 3127 (2000).

18. Lee, J. H. *et al.* Study of vertical Si/SiO<sub>2</sub> interface using laser-assisted atom probe tomography and transmission electron microscopy. *Micron* **58**, 32–37 (2014).
19. Kwak, C.-M., Seol, J.-B., Kim, Y.-T. & Park, C.-G. Laser-assisted atom probe tomography of four paired poly-Si/SiO<sub>2</sub> multiple-stacks with each thickness of 10nm. *Appl. Surf. Sci.* **396**, 497–503 (2017).
20. Larson, D. J., Geiser, B. P., Prosa, T. J. & Kelly, T. F. On the Use of Simulated Field-Evaporated Specimen Apex Shapes in Atom Probe Tomography Data Reconstruction. *Microsc. Microanal.* **18**, 953–963 (2012).
21. Seol, J.-B., Kwak, C.-M., Kim, Y.-T. & Park, C.-G. Understanding of the field evaporation of surface modified oxide materials through transmission electron microscopy and atom probe tomography. *Appl. Surf. Sci.* **368**, 368–377 (2016).
22. Kelly, T. F., Miller, M. K., Rajan, K. & Ringer, S. P. Atomic-Scale Tomography: A 2020 Vision. *Microsc. Microanal.* **19**, 652–664 (2013).
23. Loo, R. *et al.* Processing Technologies for Advanced Ge Devices. *ECS J. Solid State Sci. Technol.* **6**, P14–P20 (2017).
24. Vincent, B. *et al.* Selective Growth of Strained Ge Channel on Relaxed SiGe Buffer in Shallow Trench Isolation for High Mobility Ge Planar and Fin p-FET. *ECS Trans.* **50**, 39–45 (2013).
25. Thompson, K. *et al.* In situ site-specific specimen preparation for atom probe tomography. *Ultramicroscopy* **107**, 131–139 (2007).
26. Vurpillot, F., Cerezo, A., Blavette, D. & Larson, D. J. Modeling Image Distortions in 3DAP. *Microsc. Microanal.* **10**, 384–390 (2004).
27. Vurpillot, F. & Oberdorfer, C. Modeling Atom Probe Tomography: A review. *Ultramicroscopy* **159**, 202–216 (2015).
28. Grenier, A. *et al.* Three dimensional imaging and analysis of a single nano-device at the ultimate scale using correlative microscopy techniques. *Appl. Phys. Lett.* **106**, 213102 (2015).

29. R. Gomer, *Field Emission and Field Ionisation*. (1961).
30. Oberdorfer, C. & Schmitz, G. On the Field Evaporation Behavior of Dielectric Materials in Three-Dimensional Atom Probe: A Numeric Simulation. *Microsc. Microanal.* **17**, 15–25 (2011).
31. Geiser, B. P., Kelly, T. F., Larson, D. J., Schneir, J. & Roberts, J. P. Spatial Distribution Maps for Atom Probe Tomography. *Microsc. Microanal.* **13**, 437–447 (2007).
32. Wilkes, T. J., Smith, G. D. W. & Smith, D. A. On the quantitative analysis of field-ion micrographs. *Metallography* **7**, 403–430 (1974).
33. Gault, B., Moody, M. P., Cairney, J. M. & Ringer, S. P. *Atom Probe Microscopy*. **160**, (Springer New York, 2012).
34. Sauvage, X. *et al.* Solid state amorphization in cold drawn Cu/Nb wires. *Acta Mater.* **49**, 389–394 (2001).
35. De Geuser, F. *et al.* An improved reconstruction procedure for the correction of local magnification effects in three-dimensional atom-probe. *Surf. Interface Anal.* **39**, 268–272 (2007).
36. Richard, O., Vincent, B., Favia, P., Lagrain, P. & Bender, H. SiGe epitaxially grown in nano-trenches on Si substrate. *J. Phys. Conf. Ser.* **471**, 012028 (2013).